Materials Research Bulletin 204 (2026) 114282

Contents lists available at ScienceDirect

Materials Research Bulletin

journal homepage: www.elsevier.com/locate/matresbu

Research Papers

Multifunctional magnetic–luminescent hybrid ink with dual upconversion and downshifting lanthanide(III) emissions for anti-counterfeiting technologies

André Lucas Costa [a,b], Caique Moureira Tavares [a,b], Clara Johanna Pacheco [c], Julieth Caro Patiño [c,d], Angelo Márcio de Souza Gomes [d], Camilo Segura [e], Igor Orlando Osorio-Román [f], Flavia Artizzu [g], Sergio Antonio Marques Lima [a,b], Airton Germano Bispo-Jr [h,*], Ana Maria Pires [a,b,**]

[a] São Paulo State University (Unesp), School of Technology and Sciences, Presidente Prudente, SP 19060–900, Brazil
[b] São Paulo State University (Unesp), Institute of Biosciences, Humanities and Exact Sciences, São José do Rio Preto, SP 15054–000, Brazil
[c] Rio de Janeiro State University (UERJ), Institute of Physics Armando Dias Tavares, R. São Francisco Xavier 524, Block F, 3rd Floor, Maracanã, Rio de Janeiro, RJ 20550–013, Brazil
[d] Federal University of Rio de Janeiro (UFRJ), Low Temperature Laboratory, Institute of Physics, Av. Athos da Silveira Ramos 149, Technology Center, Bl. A, Room 427, Rio de Janeiro, RJ 21941–909, Brazil
[e] University of Chile (UChile), Faculty of Sciences, Department of Chemistry, Las Palmeras 3425, Ñuñoa, Santiago 7800003, Chile
[f] University Austral of Chile (UACh), Faculty of Sciences, Institute of Chemistry Sciences, Rector Eduardo Morales 33, Valdivia 5090000, Chile
[g] University of Piemonte Orientale "Amedeo Avogadro", Department of Sustainable Development and Ecological Transition, Vercelli, VC 13100, Italy
[h] University of São Paulo (USP), Institute of Chemistry, Lineu Prestes Street, 748, São Paulo 05508–900, Brazil

ARTICLE INFO

Keywords:
Multifunctional platform
Magnetite
Tunable emission
Core-shell

ABSTRACT

We report a stepwise strategy for synthesizing a multifunctional $Fe_3O_4/Y_{1.76}Yb_{0.2}Er_{0.04}O_3@SiO_2$-[Eu(dbm)$_3$(pamba)] hybrid (dbm: 1,3-diphenyl-1,3-propanedione, pamba: 4-(aminomethyl)benzoic acid-derived ligand) combining magnetic responsiveness with dual downshifting/upconversion luminescence for security ink applications. The architecture was assembled through Fe_3O_4 co-precipitation, homogeneous precipitation of the Y_2O_3:Yb^{3+}/Er^{3+} shell, silica coating, and surface functionalization with isocyanate groups followed by carboxylic acid grafting. Carboxylate groups were coordinated to Eu^{3+}, while dbm^- ligands occupied the remaining coordination positions, promoting efficient sensitization of Eu^{3+} luminescence. The final hybrid retained soft-magnetic behavior (Ms = 0.89 g^{-1}; negligible coercivity), exhibited strong orange upconversion under 980 nm excitation from Yb^{3+}/Er^{3+} centers and intense Eu^{3+} downshifting emission under 340 nm excitation (intrinsic quantum yield = 52%), and yielded a PVA-based multifunctional ink preserving luminescent duality and magnetic response. This system demonstrates the versatility of multifunctional magnetic nanoparticle/lanthanide hybrid platforms for next-generation security ink systems and devices in advanced anti-counterfeiting applications.

1. Introduction

Counterfeiting represents a significant global challenge with substantial implications for economic stability and public security. In 2022, financial losses associated with counterfeit U.S. dollars were estimated at approximately USD 80 million, while forged checks alone resulted in more than USD 20 billion in damages within the United States [1–3]. Commonly counterfeited items include coins, checks, banknotes [1], artworks, legal and criminal documents [4,5], and packaging for high-value goods [6], all of which require stringent authentication procedures. The continuous evolution of counterfeiting techniques, driven by increasingly sophisticated fabrication tools and digital

* Corresponding author.
** Correspondence to: São Paulo State University (Unesp), School of Technology and Sciences, R. Roberto Simonsen, 305, Presidente Prudente, SP 19060–900, Brazil.
E-mail addresses: airton.bispo.junior@iq.usp.br (A.G. Bispo-Jr), ana.maria@unesp.br (A.M. Pires).

https://doi.org/10.1016/j.materresbull.2026.114282
Received 13 March 2026; Received in revised form 20 May 2026; Accepted 3 June 2026
Available online 4 June 2026

printing technologies, highlights the urgent need for innovative, robust, and reliable anti-counterfeiting solutions [7].

The anti-counterfeiting and forensic fields have increasingly turned to advanced materials designed to enhance both security and information protection. Technologies such as plasma processing, holographic patterns, magnetic inks, and luminescent systems have been widely explored for these purposes [8]. Among them, luminescent materials have received particular attention due to their distinctive emission features, including multicolor outputs, tunable lifetimes ranging from milliseconds to nanoseconds, and sensitivity to external stimuli such as light, heat, or electric fields. These properties enable the development of highly secure optical tags and encryption systems that are difficult to replicate [9]. Rare earth ions (RE^{3+}) have attracted significant interest in the formulation of security inks owing to their remarkable photophysical characteristics, such as sharp emission bands, long-lived excited states, high color purity, and tunable visible and near-infrared emissions [10–15]. Recent advances have demonstrated the versatility of RE^{3+}-doped systems in multifunctional anti-counterfeiting technologies, enabling the integration of optical encoding, stimulus-responsive behavior, and advanced information protection within a single material architecture [16,17]. Representative examples, together with the systems summarized in Table 1, highlight the growing interest in RE^{3+}-based platforms [18–20].

In this context, inorganic-organic hybrids doped with RE^{3+} ions have emerged as promising platforms for luminescent anti-counterfeiting applications, as these materials can be formulated as security inks and incorporated into authentication labels, encrypted barcodes, and QR codes [21]. Their combination of sharp emission profiles, high chemical and thermal stability, low toxicity, and straightforward synthesis, results in desirable optical performance and enhances the reliability of authentication technologies [22]. Notably, formulations based on Y_2O_3:Eu^{3+} phosphors dispersed in poly(vinyl alcohol) (PVA) have shown potential for luminescent signature hand-drawn, offering inherent resistance to replication and excellent durability [23,24]. PVA further provides additional advantages such as an environmentally friendly and non-toxic polymer matrix, which is particularly relevant when security inks are intended for direct human contact or for hand-drawn on sensitive surfaces [24].

The integration of magnetic and luminescent functionalities represents a promising avenue toward multimodal anti-counterfeiting systems. Magnetic inks based on ferrite or Fe_3O_4 nanoparticles are employed in Magnetic Ink Character Recognition (MICR) since they can generate instantaneous, high-resolution magnetic responses under controlled magnetic fields, enabling rapid retrieval, identification, and quantitative analysis of encoded information [25,26]. When applied to documents such as bank cheques or payment vouchers, the hand-drawn characters can be automatically read and authenticated using MICR readers [26,27]. As example, recent studies have demonstrated that silicon-based nanostructured security inks can achieve dual-encryption performance through the combination of multicolor fluorescence and longitudinal (T_1) and transverse (T_2) relaxation contrast [25]. Nevertheless, despite these advances, most reported systems remain predominantly limited to optical responses or require complex activation processes, while relatively few materials simultaneously combine magnetic responsiveness, visible and near-infrared luminescence, thermal stability, and direct applicability as stable drawn inks.

Building upon these advancements, the present study introduces a multifunctional magnetic-luminescent core@shell architecture that integrates both upconversion and downshifting emission within a single magnetic framework [28]. Based on a previously established synthetic protocol [29], the system reported here consists of a magnetic Fe_3O_4 core, a Y_2O_3:Yb(10 at%)Er(2 at%) upconverting phosphor shell, and an outer silica layer functionalized with [Eu(dbm)$_3$(pamba)] downshifting complex

(dbm^-: 3-diphenyl−1,3-propanedione; pamba: 4-(aminomethyl) benzoic acid derivative), as illustrated in Fig. 1. When dispersed in a PVA polymer matrix, this architecture enables magnetic responsiveness and dual-mode luminescence as a function of the excitation wavelength.

Table 1
Comparison of representative multifunctional anti-counterfeiting materials reported in recent literature, including their main advantages and limitations relative to the $Fe_3O_4/Y_{1.76}Yb_{0.20}Er_{0.04}O_3$@$SiO_2$-[Eu(dbm)$_3$(pamba)] hybrid developed in this work.

Material/System	Advantages	Limitations
BiOCl:Yb^{3+}/Ho^{3+}[18]	Dynamic and rewritable anti-counterfeiting; multiple optical responses; concealment, activation, and erasure capability.	No magnetic functionality; response strongly dependent on external photoactivation processes.
$[SbCl_6]^{3-}$ to Ln^{3+} (Ln^{3+} = Ho^{3+}, Er^{3+}) in $Cs_2NaGdCl_6$ [19]	Multicolor emission; stimulus-responsive behavior; efficient STE→Ln^{3+} energy transfer.	Moisture sensitivity may limit long-term environmental stability; no magnetic response.
$Bi_2Ti_4O_{11}$:Yb^{3+},Er^{3+}@TPU thermoplastic polyurethane (TPU)[20]	Flexible and stretchable substrate compatibility; waterproof and transparent films	Primarily optical authentication; absence of magnetic encoding.
Fe_3O_4/$Y_{1.76}Yb_{0.20}Er_{0.04}O_3$@$SiO_2$-[Eu(dbm)$_3$(pamba)] (this work)	Combines optical and magnetic authentication in a single platform; dual excitation-dependent emission and thermal stability; compatible with ink formulations.	Partial nanoparticle aggregation observed in TEM images.

2. Results and discussion

2.1. Structure and morphology

The samples were synthesized following a protocol previously reported by our group for the preparation of Fe_3O_4 + Y_2O_3:Yb^{3+}, Tm^{3+}@SiO_2-[Eu(4-Cl-btfa)$_3$(pamba)] with 1-(4-chlorophenyl)−4,4,4-trifluoro−1,3-butanedione (4-Cl-btfa) ligand [29], as detailed in Supplementary Note S1. To ensure practical feasibility for anti-counterfeiting applications, the upconverting phosphor $Y_{1.76}Yb_{0.20}Er_{0.04}O_3$ was deposited onto Fe_3O_4 magnetic nanoparticles (sample S01), yielding the composite $Fe_3O_4/Y_{1.76}Yb_{0.20}Er_{0.04}O_3$ (sample S02). The selection of Er^{3+} as the luminescent activator instead of Tm^{3+} was motivated by its intense green and red upconversion emissions, which provide highly distinguishable and robust optical signatures.

In the second coating step, a dense silica layer was deposited, yielding $Fe_3O_4/Y_{1.76}Yb_{0.20}Er_{0.04}O_3$ @SiO_2 (S03). The silica surface was first functionalized with isocyanate (-NCO) groups using 3-(triethoxysilyl)propyl isocyanate as the silane precursor, yielding $Fe_3O_4/Y_{1.76}Yb_{0.20}Er_{0.04}O_3$ @SiO_2-NCO (S04). Subsequently, the ligand 4-(aminomethyl)benzoic acid (pamba), bearing both an amino (-NH_2) and a carboxylic acid (-COOH) group, was covalently anchored onto the surface via reaction of its -NH_2 moiety with the surface -NCO groups, affording $Fe_3O_4/Y_{1.76}Yb_{0.20}Er_{0.04}O_3$@$SiO_2$-pamba (S05). Eu^{3+} ions were then coordinated to the terminal -COO^- groups of the grafted organic ligand, referred to here as pamba, and their coordination spheres were completed with the β-diketonate ligand 1,3-diphenylpropane-1,3-dionate (dbm^-). This process yielded the final materials $Fe_3O_4/Y_{1.76}Yb_{0.20}Er_{0.04}O_3$@$SiO_2$-[Eu(pamba)$(H_2O)_n$] (S06) and $Fe_3O_4/Y_{1.76}Yb_{0.20}Er_{0.04}O_3$@$SiO_2$-[Eu(dbm)$_3$(pamba)] (S07). The dbm^- ligand promotes efficient ligand-to-Eu^{3+} intramolecular energy transfer via the antenna effect, resulting in intense downshifting luminescence. Additional synthesis and characterization details are provided in

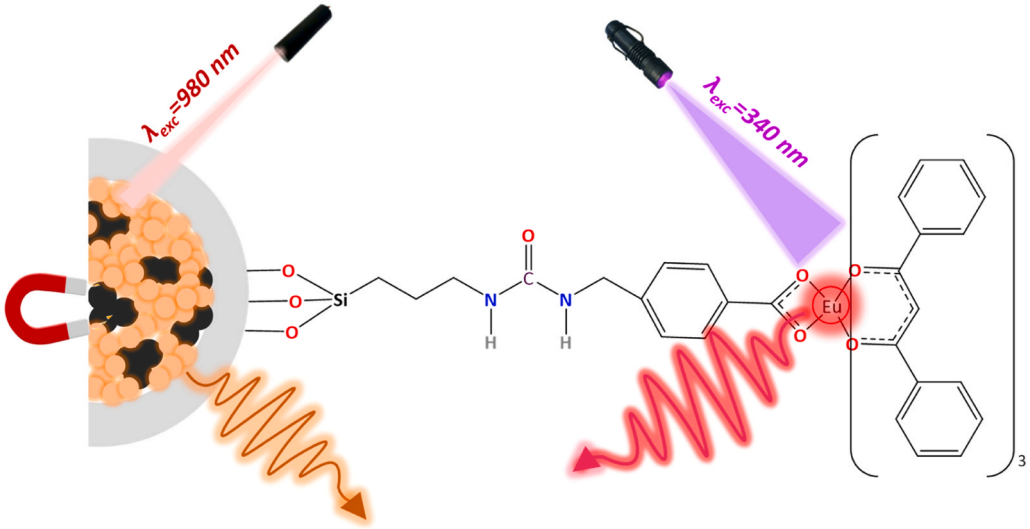

Fig. 1. Schematic representation of the multifunctional hybrid system based on a $Fe_3O_4/Y_{1.76}Yb_{0.20}Er_{0.04}O_3$@$SiO_2$ core@shell architecture functionalized with the [Eu(dbm)$_3$(pamba)] complex. The illustration is not drawn to scale and does not represent the actual dimensions of the hybrid material.

Supplementary Note S1.

The successful formation of Fe_3O_4 and $Y_{1.76}Yb_{0.20}Er_{0.04}O_3$ phases was confirmed by powder X-ray diffraction (PXRD), Fig. S1. Fe_3O_4 crystallizes in the inverse spinel structure with space group *Fd-3m* [30], while $Y_{1.76}Yb_{0.20}Er_{0.04}O_3$ adopts a cubic structure with space group *Ia−3* [31] Fig. S2. The absence of additional diffraction peaks indicates that Yb^{3+} and Er^{3+} were successfully incorporated into the Y_2O_3 lattice [32], which is consistent with the similar ionic radii of Y^{3+} (0.90 Å), Yb^{3+} (0.87 Å), and Er^{3+} (0.89 Å) in octahedral coordination [33,34]. It should be noted that the reflections associated with the Fe_3O_4 phase are not observed in the PXRD pattern of sample S02 (Fig. S1). This is attributed to the large phosphor-to-magnetite mass ratio (100:1), together with the nanometric size of the Fe_3O_4 nanoparticles, which results in significant peak broadening [35,36]. Moreover, the weak magnetite reflections are largely marked by the intense diffraction peaks of the $Y_{1.76}Yb_{0.20}Er_{0.04}O_3$ phosphor [37,38].

Surface chemical modifications were monitored by Fourier-transform infrared (FTIR) spectroscopy (Fig. S3). For sample S02, the broad band in the 500–600 cm^{-1} region is characteristic of metal-oxygen vibrational modes (Fe-O). This stretching vibration arises from both tetrahedral (A-side) and octahedral (B-side) coordination environments [39]. Lower-frequency vibrational modes are consistent with Y-O lattice vibrations [40], indicating successful incorporation of the Y_2O_3 phase; the broad nature of those bands is typical of nanocrystalline oxides. After silica coating (S03), IR bands appeared at 1068 cm^{-1}, 950 cm^{-1}, and 790 cm^{-1}; the bands at ~1068 cm^{-1} and 790 cm^{-1} are assigned to Si–O–Si antisymmetric and symmetric stretching, respectively. In addition, Si–O–Si bending vibration is detected near 450 cm^{-1}. The presence of Si-OH stretching band at 950 cm^{-1}, together with the other three IR bands, confirms the formation of silica shell [41].

The functionalization with pamba (S05) led to the emergence of bands at 1540 cm^{-1}, 1460 cm^{-1}, and 1364 cm^{-1}, assigned to the antisymmetric and symmetric stretching modes of carboxylate groups (Fig. S3) [42,43]. After anchoring the Eu^{3+} complex (S07), further vibrational bands appeared between 1600–1450 cm^{-1} region, characteristic of the aromatic vibrations of dbm^- ligand, together with bands in the 1250–1100 cm^{-1} range, associated with C–O and C–C stretching modes [44]. Overall, the systematic evolution of the IR spectra provides compelling evidence of sequential surface chemistry modification, thereby confirming the stepwise functionalization of the hybrid nanostructure.

Zeta potential (ZP) measurements for samples suspended in water (pH = 7.64) further corroborated the systematic surface modifications (Fig. S4). Each synthetic step induced predictable changes in the electrokinetic potential, consistent with the evolving surface chemistry previously reported by us [29]. The $Y_{1.76}Yb_{0.20}Er_{0.04}O_3$ particles (S02) exhibited a positive surface charge and high isoelectric point (IEP). Upon silica deposition, the ZP shifted towards negative values and subsequently evolved in a manner consistent with the successive surface functionalization steps [45].

The morphology of the intermediate materials was investigated by scanning electron microscopy (SEM) and transmission electron microscopy (TEM). The SEM image (Fig. S5) reveals spherical Fe_3O_4 nanoparticles (S01) with an average diameter of approximately 29 nm and homogenous size distribution. TEM images (Fig. 2a) display well-defined lattice fringes corresponding to the crystallographic planes of magnetite, confirming the high crystallinity of the material [46]. The interplanar spacings measured from these images, summarized in Table S1, are in good agreement with the expected values for Fe_3O_4. In addition, the energy dispersive X-ray spectroscopy (EDS) analysis (Fig. S6) confirms the presence of Fe and O in proportions consistent with stoichiometric magnetite [47,48].

Following the growth of the $Y_{1.76}Yb_{0.20}Er_{0.04}O_3$ layer (S02), the TEM image (Fig. 2b) reveals additional lattice fringes assigned to the cubic Y_2O_3 phase, confirming the presence of the phosphor and its high crystallinity. Sample S03 exhibits a slight tendency toward aggregation (Fig. 2c), a behavior commonly observed in materials subjected to sequential surface functionalization. High-resolution TEM further reveals the presence of a non-crystalline outer layer with an average thickness of approximately 4.7 nm, which is assigned to the SiO_2 shell, in agreement with the FTIR results [49]. The EDS spectrum (Fig. S7) qualitatively indicates the presence of yttrium, ytterbium, silicon, and iron, consistent with the expected elemental composition of the composite, further supporting the successful formation of the nanocomposite. Importantly, the crystallographic planes detected in S03 can be indexed to both Fe_3O_4 and Y_2O_3, indicating that the crystallinity of both phases is preserved after silica deposition [50].

It is important to note that due to the aggregation observed after the coating steps, the system presents a multicore@shell-like morphology, in which multiple $Fe_3O_4/Y_{1.76}Yb_{0.20}Er_{0.04}O_3$ cores are embedded within a continuous silica matrix. Additionally, the low contrast of the amorphous SiO_2 layer and the similar electron densities of the inorganic phases hinder the direct visualization of well-defined interfaces in TEM images. Nevertheless, the presence of a non-crystalline outer layer surrounding crystalline domains, together with complementary evidence from FTIR, zeta potential, EDS, and PXRD analyses, supports the

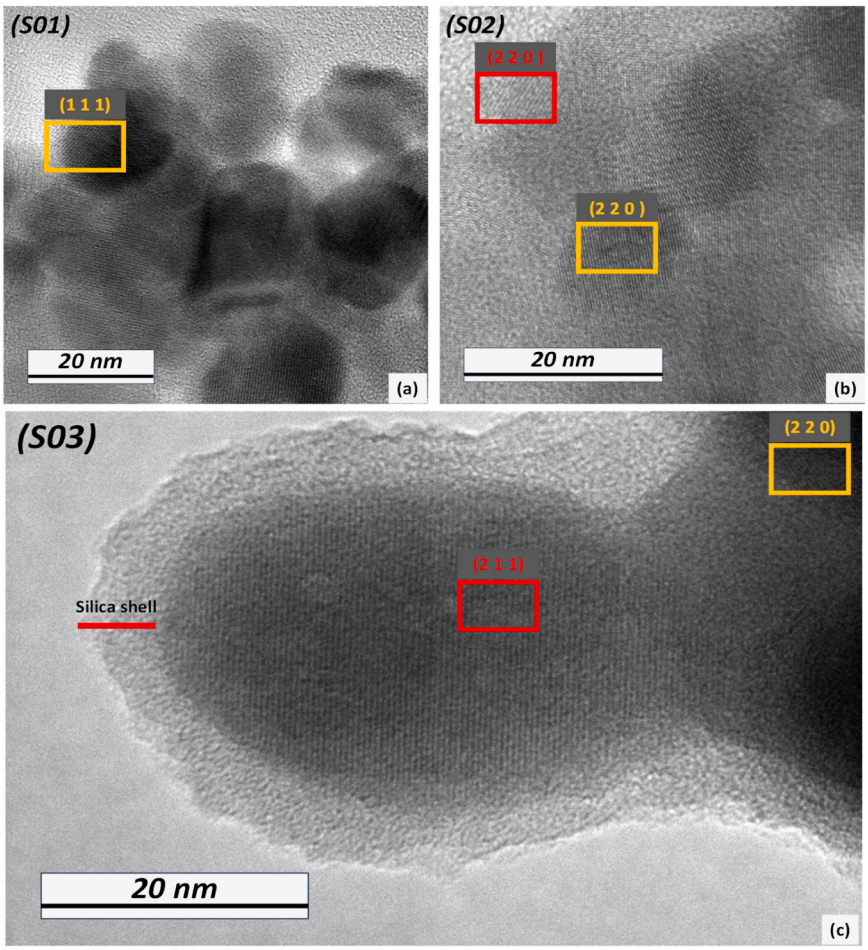

Fig. 2. High-resolution TEM (HRTEM) images of the samples: (a) Fe_3O_4 nanoparticles (S01), showing indexed (111) lattice fringes characteristic of the magnetite phase; (b) $Fe_3O_4/Y_{1.76}Yb_{0.20}Er_{0.04}O_3$ (S02) highlighting the indexed (220) plane of Fe_3O_4 and the (222) plane of Y_2O_3; (c) $Fe_3O_4/Y_{1.76}Yb_{0.20}Er_{0.04}O_3@SiO_2$ (S03), displaying the (220) reflection of Fe_3O_4, the (211) reflection of Y_2O_3, and a non-crystalline silica shell. The crystallographic planes were selected from representative regions of the HRTEM images for Miller index assignment.

successful formation of silica-coated hybrid structures consistent with a multicore@shell architecture.

2.2. Magnetic properties

The magnetic behavior of the materials was evaluated at 300 K through magnetization (M vs. H) measurements. The magnetization curve follows the same trend observed for the analogous $Fe_3O_4 + Y_2O_3$: Yb,Tm@SiO_2 hybrid systems [29], which exhibited low saturation magnetization and negligible coercivity at room temperature due to the diamagnetic contribution of the coated layers (Fig. 3a and b). In the present study, the Fe_3O_4 core (S01) (Fig. 3c and d), shows a clear ferrimagnetic hysteresis loop at 300 K, with a saturation magnetization of 68.37 g^{-1} and a coercivity of 81.49 Oe, confirming the presence of stable magnetic domains in the uncoated magnetite [51–53]. The pronounced magnetic response is typical of nanoscale Fe_3O_4 and consistent with well-crystallized inverse spinel magnetite cores. After coating with the upconverting $Y_{1.76}Yb_{0.2}Er_{0.04}O_3$ @SiO_2 phosphor and silica shell (S03), ferrimagnetic behavior is retained (Fig. 3b), although with markedly reduced magnetic parameters (M_s = 0.89 g^{-1} and H_c = 13.29 Oe). This decrease is mainly attributed to the dilution effect caused by the diamagnetic silica shell and rare-earth oxide layer, a trend widely reported for Fe_3O_4-based core@shell architectures [54,55]. The reduced coercivity further reflects the partial suppression of interparticle magnetic coupling due to the physical separation introduced by the silica coating.

Despite the pronounced decrease in magnetization, S03 maintains a measurable magnetic response at 300 K, indicating that the phosphor and silica coatings are sufficiently thin so that the core's ferrimagnetism is not completely quenched. Taken together, these results confirm that the synthetic procedure yields a Fe_3O_4-based core@shell system with preserved magnetic behavior.

2.3. Luminescent properties

After confirming the successful synthesis of the hybrid material and the preservation of its magnetic properties, the luminescent behavior of the final composition (S07) was investigated. Figure 4a shows the upconversion spectrum of S07 under 980 nm laser excitation (500 mW). The two emission bands in the green spectral region are attributed to the Er^{3+} $^2H_{11/2}$,$^4S_{3/2}\rightarrow{}^4I_{15/2}$ transitions, whereas the dominant emission band in the red spectral range arises from the Er^{3+} $^4F_{9/2}\rightarrow{}^4I_{15/2}$ transition [56,57].

Fig. S8 shows the dependence of the Er^{3+} emission intensity on the excitation power. The intensity of both green ($^2H_{11/2}$,$^4S_{3/2}\rightarrow{}^4I_{15/2}$) and red ($^4F_{9/2}\rightarrow{}^4I_{15/2}$) emissions increases with increasing laser power, exhibiting the characteristic behavior of upconversion systems [58]. In the 500–1000 mW range, the slope of the *log I* vs. *log P* plot is close to 2 (Fig. S9), indicating a two-photon process. This result is consistent with the $I \alpha P^n$ dependency, where I is the emission intensity, P is the excitation power, and n corresponds to the number of photons involved in the upconversion mechanism [59]. The observed behavior agrees with

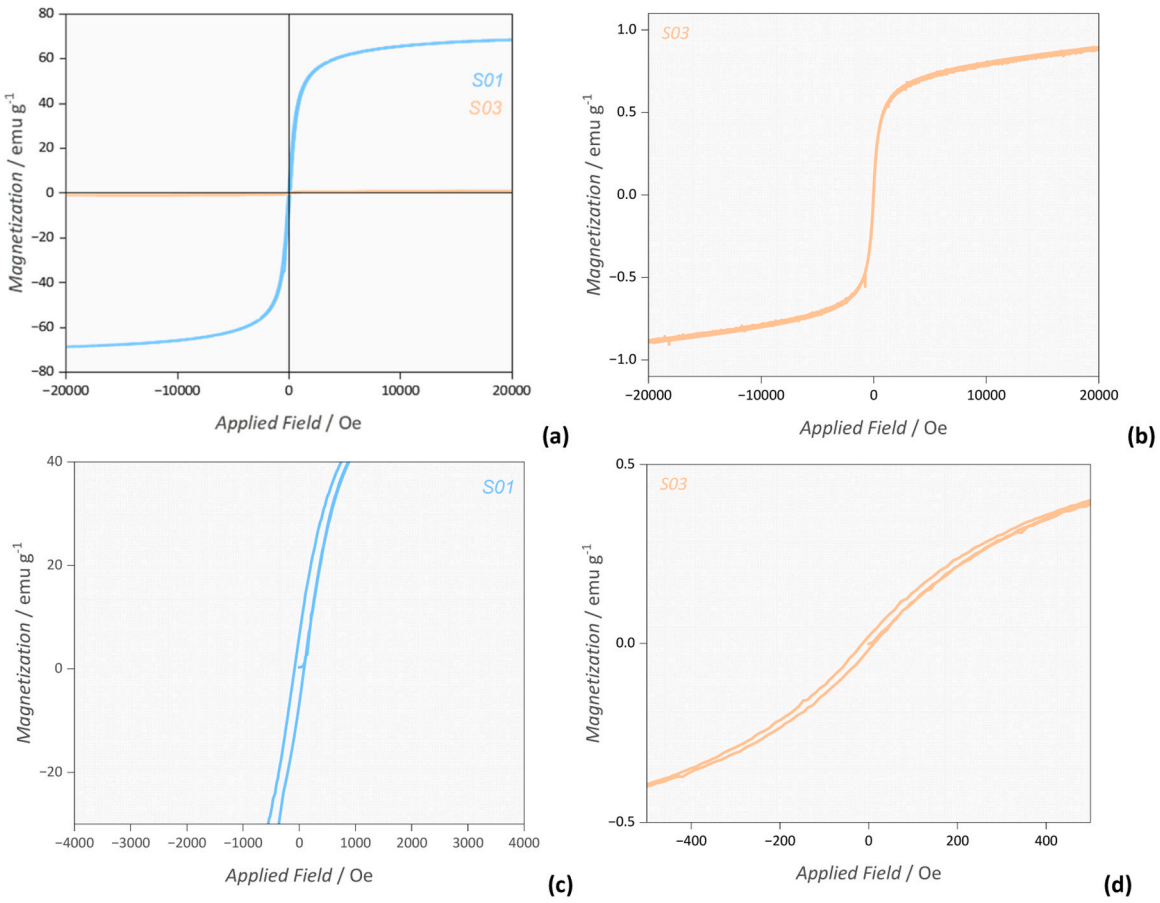

Fig. 3. (a) Magnetic hysteresis loops of Fe_3O_4 (S01) and $Fe_3O_4/Y_{1.76}Yb_{0.20}Er_{0.04}O_3@SiO_2$ (S03) measured at 300 K. (b) Magnetic hysteresis loops of $Fe_3O_4/Y_{1.76}Yb_{0.20}Er_{0.04}O_3@SiO_2$ (S03) measured at 300 K. Magnification of the magnetic hysteresis loops (c) Fe_3O_4 (S01) and (d) $Fe_3O_4/Y_{1.76}Yb_{0.20}Er_{0.04}O_3@SiO_2$ (S03) measured at 300 K.

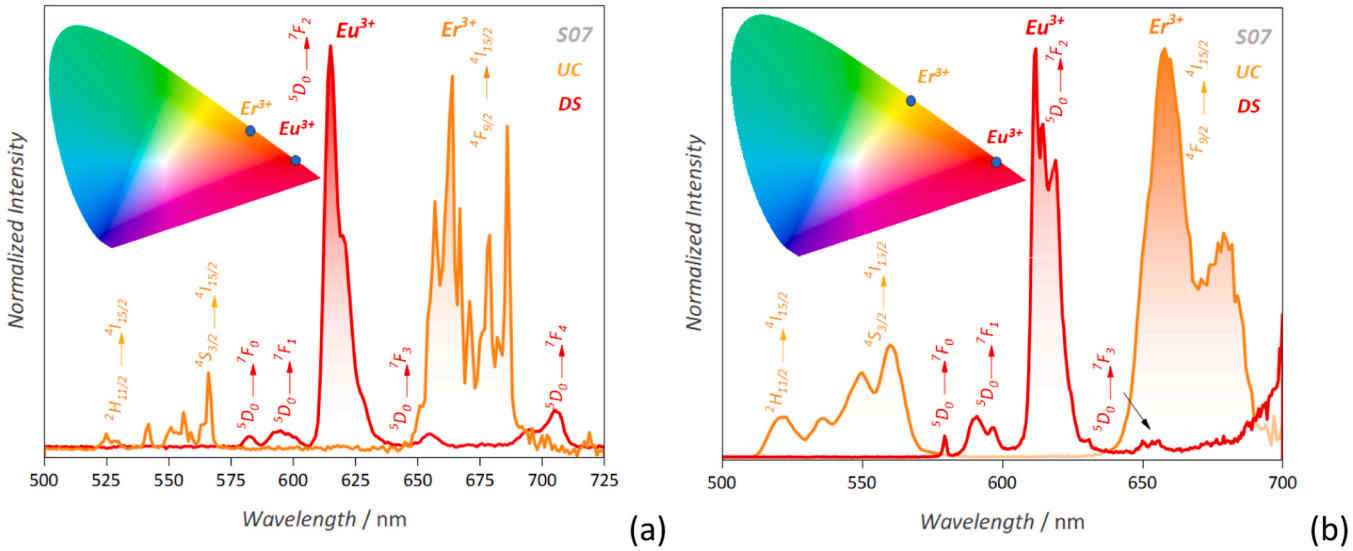

Figure 4. 298 K upconversion emission spectrum (UC) under 980 nm excitation (500 mW) and downshifting emission spectrum (DS) (λ_{exc} = 340 nm) of $Fe_3O_4/Y_{1.76}Yb_{0.20}Er_{0.04}O_3@SiO_2$-[$Eu(dbm)_3(pamba)$] (S07) as (a) powder or (b) PVA ink. The insect shows the corresponding CIE 1931 chromaticity diagram, highlighting the emission coordinates associated with Er^{3+} upconversion and Eu^{3+} downshifting luminescence.

the typical $Yb^{3+}\rightarrow Er^{3+}$ upconversion pathway, in which Yb^{3+} acts as efficient sensitizer by absorbing NIR radiation and transferring energy sequentially to Er^{3+} ions. These successive energy-transfer steps populate higher excited states of Er^{3+}, followed by nonradiative relaxation to the $^2H_{11/2}$, $^4S_{3/2}$ and $^4F_{9/2}$ emitting levels, giving rise to the observed green and red emissions (Fig. S10) [60,61].

After analyzing the Er^{3+}/Yb^{3+} upconversion process, the downshifting luminescence of the Eu^{3+} complex anchored on the particle

surface was investigated. The excitation spectrum monitored at the Eu^{3+} emission (Fig. S11) shows a broad absorption band between 330–400 nm region, which is attributed to the π-π* transition of the β-diketonate dbm^- ligand. This feature provides clear evidence of the antenna effect operating in the hybrid system, whereby the organic ligand efficiently absorbs UV radiation and transfers the energy to Eu^{3+} ions, resulting in enhanced Eu^{3+} emission [44,62].

In the emission spectrum of $Fe_3O_4/Y_{1.76}Yb_{0.20}Er_{0.04}O_3$@$SiO_2$-[Eu(dbm)$_3$(pamba)], Figure 4a, recorded under 340 nm excitation, sharp emission bands are observed and assigned to the Eu^{3+} $^5D_0 \rightarrow {}^7F_J$ ($J = 0$–4) transitions, confirming the presence of Eu^{3+} complexes anchored onto the silica surface. The hypersensitive $^5D_0 \rightarrow {}^7F_2$ transition dominates the spectrum, resulting in intense red emission, which indicates that Eu^{3+} ions are in low-symmetry coordination sites lacking an inversion center. This behavior is consistent with coordination environments involving mixed ligands, such as carboxylate and β-diketones groups [63,64].

The emission colors of S07 were evaluated by the CIE 1931 chromaticity diagram (Fig. 4a), while additional details regarding the calculation are provided in Supplementary Note S8. Under NIR excitation (980 nm), the chromaticity coordinate is positioned in the orange region of the diagram, exhibiting a dominant wavelength (λ_{dom}) of 585.4 nm and a color purity of 99.1%. This emission originates from the Er^{3+} upconversion emission sensitized by Yb^{3+} ions. Conversely, under UV excitation (λ_{exc} = 340 nm), the chromaticity coordinate shifts toward the red region, with λ_{dom} = 609.6 nm and a color purity of 99.6%, corresponding to the characteristic Eu^{3+} downshifting emission. These results demonstrate the dual-mode luminescent behavior of $Fe_3O_4/Y_{1.76}Yb_{0.20}Er_{0.04}O_3$@$SiO_2$-[Eu(dbm)$_3$(pamba)] (S07), in which the emission color can be selectively modulated by the excitation wavelength, highlighting its potential for advanced anti-counterfeiting and optical encoding applications.

The photophysical dynamics of lanthanide(III) luminescence in S07 was investigated by time-resolved spectroscopy. The decay profiles of the Er^{3+} emission monitored under 980 nm excitation (Fig. S12a, b and c), corresponding to the $^2H_{11/2}$, $^4S_{3/2}$, and $^4F_{9/2}$ excited levels, are described by mono-exponential functions. This behavior indicates a dominant relaxation pathway for Er^{3+} ions, suggesting a relatively homogeneous local environment within the Y_2O_3-based host lattice [65]. The extracted lifetimes are 0.20 ms for the $^2H_{11/2}$ level, 0.18 ms for the $^4S_{3/2}$ level, and 0.19 ms for the $^4F_{9/2}$ level. These values are consistent with those typically reported for Er^{3+}-doped oxide and hybrid matrices [66,67].

The decay profile of the Eu^{3+} emission sensitized via the antenna effect is best fitted by a biexponential function, indicating the coexistence of two distinct Eu^{3+} emissive environments, Fig. S12d. The shorter lifetime component, (τ_1 = 0.18 ms), is associated with Eu^{3+} centers more strongly coupled with high-energy vibrational oscillators (O-H, N-H, or C-H), which enhance nonradiative relaxation, likely due to partial coordination by water molecules. In contrast, the longer lifetime component (τ_2 = 0.45 ms) is attributed to Eu^{3+} ions in more shielded coordination environments, consistent with coordination by β-diketonate ligands [68–71]. The resulting average lifetime was determined to be $\bar{\tau}$ = 0.37 ms.

To further elucidate the balance between radiative and nonradiative pathways governing the depopulation of the Eu^{3+} $^5D_0$ emissive level, the intrinsic emission quantum yield (ϕ_{Eu}^{Eu}) was determined as the ratio between the radiative decay rate (A_{rad}) and the total decay rate, as defined in Eqn (S2). Details of the calculations are provided in Supplementary Note S10 [72]. The $Fe_3O_4/Y_{1.76}Yb_{0.20}Er_{0.04}O_3$@$SiO_2$-[Eu(dbm)$_3$(pamba)] hybrid exhibits an intrinsic quantum yield of 52%, which is a consequence of the relatively high radiative decay rate (A_{rad} = 1408.89 s^{-1}) and balanced nonradiative contribution (A_{nrad} = 1293.81 s^{-1}). The intrinsic emission quantum yield is consistent with those typically reported for Eu^{3+} β-diketonate-based hybrids (≈40–70%) [73,74], evidencing that the coordination environment provided by the dbm^- and pamba ligands, together with the rigid SiO_2 framework, effectively reduces vibrational quenching and favors bright Eu^{3+} luminescence [75].

2.4. Luminescent inks

Based on the results presented and discussed above, a luminescent PVA-based ink was prepared by incorporating the $Fe_3O_4/Y_{1.76}Yb_{0.20}Er_{0.04}O_3$@$SiO_2$-[Eu(dbm)$_3$(pamba)] hybrid, as described in Supplementary Note S1. Under UV excitation (λ_{exc} = 340 nm), the ink deposited on both glass slides and black paper exhibit intense red emission (Fig. 5). Moreover, using a 980 nm laser pointer, the characteristic upconversion emission of the ink can be readily observed by the naked eye. In contrast, under white-light illumination, the substrates remain essentially non-emissive, reflecting the optical transparency of the ink on glass and its low visual contrast on the black paper.

The luminescent performance of the ink was further confirmed by recording emission spectra under excitation at 980 nm and 340 nm, selectively addressing the Yb^{3+}/Er^{3+} upconversion process and the dbm^- sensitized Eu^{3+} downshifting emission, respectively (Fig. 4b). Under 980 nm excitation, the upconversion spectrum displays the characteristic Er^{3+} transitions $^2H_{11/2}$, $^4S_{3/2}$, and $^4F_{9/2} \rightarrow {}^4I_{15/2}$, indicating that the upconversion mechanism is preserved after dispersion in the PVA matrix. Analysis of the corresponding CIE 1931 chromaticity coordinates reveals a shift of the dominant wavelength to 571.3 nm relative to the free-standing hybrid, accompanied by slight decrease in color purity to 97.5%.

Under 340 nm excitation, the downshifting emission spectrum displays the characteristic Eu^{3+} *f-f* transitions, in agreement with the behavior observed for the hybrid in powder form. The corresponding CIE 1931 chromaticity coordinates yield a dominant wavelength of 612.0 nm and a color purity of 96.6%, slightly lower than those measured prior to incorporation into the PVA matrix. As observed for the Er^{3+} emission, this modest reduction in color purity is attributed to refractive index changes introduced by the polymeric environment, which affect light propagation and spectral balance within the medium. Overall, these results confirm that the dual-mode luminescent response is preserved after processing into an ink, underscoring the robustness of the hybrid material for anti-counterfeiting applications.

To further verify the magnetic functionality of the formulated ink, an alternative composition employing a Fe_3O_4 to $Y_{1.76}Yb_{0.20}Er_{0.04}O_3$ mass ratio of 1:50 was evaluated resulting in enhanced magnetic responsiveness. As show in Fig. 6, the magnetic-luminescent ink can be efficiently attracted and lifted by the neodymium magnet, demonstrating that the magnetic properties of the Fe_3O_4 core are preserved after surface functionalization and incorporation into the polymer matrix.

Thermogravimetric analysis (TG/DSC) of the PVA ink containing S07 (Fig. S13) was performed to evaluate the thermal behavior and thermal stability of the multifunctional formulation. The TG curve shows an initial mass loss below ~100 °C, attributed to the removal of physically adsorbed water and residual solvents. A more pronounced mass-loss process is observed between ~220 and 465 °C, associated with the progressive decomposition of the organic fraction present in the ink formulation. Above this temperature range, the mass gradually stabilizes, indicating the formation of a more thermally stable residual fraction.

The DSC curve (Fig. S13) exhibits broad thermal events throughout the heating process, reflecting the complex multicomponent nature of the formulation. A marked thermal event centered near ~465 °C is associated with the main degradation stage of the organic components, while a second broader event extending to higher temperatures indicates the progressive decomposition of the remaining constituents.

Despite this complexity, the thermal analysis demonstrates that the ink remains stable below ~150 °C, which is fully compatible with conventional coating, printing, and hand-drawn application conditions. Furthermore, the ZP values remained nearly constant over 12 h

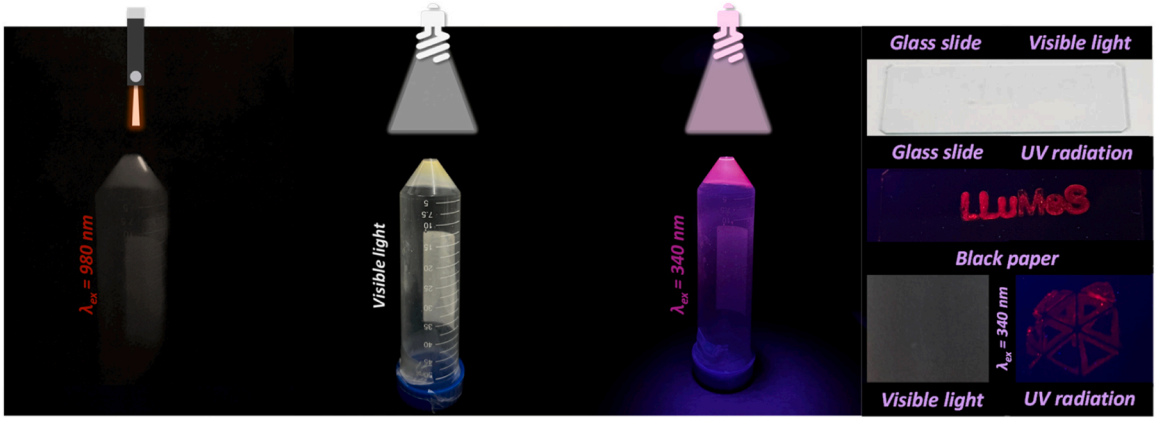

Fig. 5. Dual-excitation luminescence response of the PVA-based ink containing the $Fe_3O_4/Y_{1.76}Yb_{0.20}Er_{0.04}O_3@SiO_2$-[Eu(dbm)$_3$(pamba)] hybrid (S07). Near-infrared excitation at 980 nm (left) produces upconversion emission dominated by Er^{3+} electronic transitions, whereas ultraviolet excitation at 340 nm (right) yields intense red emission arising from energy transfer to Eu^{3+}. The central image shows the ink under white-light illumination. Images on the far right display the ink deposited on glass and black paper under visible light and UV irradiation, highlighting excitation-selective emission and contrasting luminescent hand-draw. The observed luminescent markings correspond to the acronym LLuMeS, referring to the *Laboratory of Luminescence in Materials and Sensors*, and to the official logo of São Paulo State University (*Universidade Estadual Paulista*, UNESP).

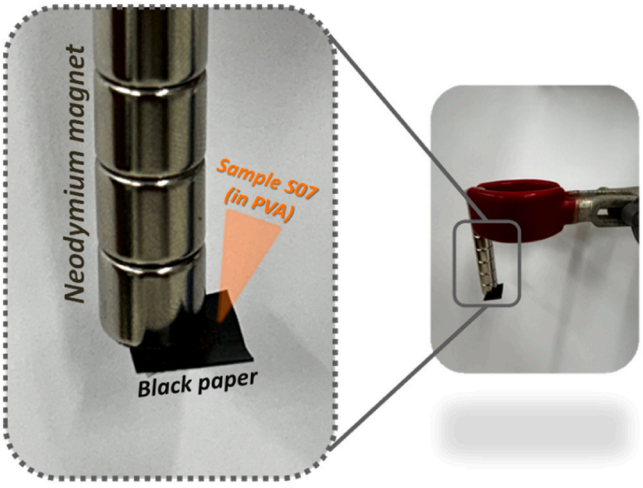

Fig. 6. Magnetic manipulation of the PVA-based ink containing the $Fe_3O_4/Y_{1.76}Yb_{0.20}Er_{0.04}O_3@SiO_2$-[Eu(dbm)$_3$(pamba)] hybrid using a neodymium magnet. The formulation employs a Fe_3O_4:$Y_{1.76}Yb_{0.20}Er_{0.04}O_3$ mass ratio of 1:50, demonstrating preserved magnetic responsiveness after functionalization and incorporation into the polymer matrix.

(Fig. S4), varying from + 2.85 to + 3.23 mV, indicating good dispersion reproducibility and satisfactory colloidal stability during both preparation and application stages. Collectively, these results support the suitability of the formulation as a multifunctional anti-counterfeiting ink for rapid authentication applications, including hand-drawn security markings and stamps.

3. Conclusion

In this work, we successfully optimized a multifunctional magnetic and luminescent hybrid system based on the $Fe_3O_4/Y_{1.76}Yb_{0.20}Er_{0.04}O_3@SiO_2$-[Eu(dbm)$_3$(pamba)] architecture. Structural and surface analyses (PXRD, FTIR, zeta potential, and EDS) confirmed the formation of the expected phases and the effectiveness of the sequential silica coating and Eu^{3+} complex functionalization. Electron microscopy revealed core@shell morphology with silica-derived non-crystalline layers, while magnetic measurements verified preservation of the ferrimagnetic behavior despite reduced saturation magnetization. The hybrid material exhibited orange upconversion emission under 980 nm excitation and red downshifting luminescence under 340 nm excitation, associated with Er^{3+} and Eu^{3+} centers, respectively. When incorporated into a PVA matrix to produce a luminescent ink, the system retained its dual-mode emission response, showing only minor shifts in dominant wavelength and color purity due to polymer-RE^{3+} ion interactions. The ink also remained magnetically responsive, enabling combined luminescent and magnetic detection. Overall, these results demonstrate robustness and versatility of this core@shell platform, highlighting its potential for multifunctional devices, particularly in security and anti-counterfeiting applications where dual-mode luminescence and magnetic responsiveness are highly desirable.

CRediT authorship contribution statement

André Lucas Costa: Writing – original draft, Validation, Methodology, Investigation, Formal analysis, Data curation, Conceptualization. **Caique Tavares:** Writing – review & editing, Methodology, Investigation, Formal analysis. **Clara Johanna Pacheco:** Writing – review & editing, Conceptualization. **Julieth Patiño:** Writing – review & editing, Formal analysis. **Angelo Márcio de Gomes:** Writing – review & editing, Formal analysis, Conceptualization. **Camilo Segura:** Writing – review & editing, Conceptualization. **Igor Orlando Osorio-Román:** Writing – review & editing, Conceptualization. **Flavia Artizzu:** Writing – review & editing, Supervision, Resources, Conceptualization. **Sergio Antonio Marques Lima :** Writing – review & editing, Supervision, Resources, Methodology, Formal analysis, Conceptualization. **Airton Bispo-Jr:** Writing – review & editing, Formal analysis, Conceptualization. **Ana Maria Pires:** Writing – review & editing, Visualization, Validation, Supervision, Resources, Project administration, Methodology, Funding acquisition, Formal analysis, Conceptualization.

Declaration of Competing Interest

Given their role as Editor of Materials Research Bulletin, Flavia Artizzu was not involved in the peer-review of this article and has no access to information regarding its peer-review. Full responsibility for the editorial process for this article was delegated to another journal editor.

Acknowledgements

This work was supported by CNPq (Brazilian Agency) through INCT-

LumiNanoTec (grant 408501/2024–3). AMP and SAM acknowledge CNPq (309448/2021–2, 305313/2024–0 and 308868/2022–6.) for the award of a productivity scholarship. ALC thanks CAPES for the award of pH.D. (88887.686388/2022–00) and PDSE (88881.934576/2024–01) scholarships. AGBJ thanks the Support Program for New Faculty at USP from PRPI – USP and FAPESP (2025/08634–6). The authors are also thankful to Laboratory of Pesticide Residue Analysis (FCT-UNESP) for the FTIR measurements, Laboratory of Nanostructured Materials for Environmental and Biological Analyses (FCT-UNESP) for the Zeta Potential measurements, and Analytical Instrumentation Center of the University of São Paulo (IQ-USP). The multi-user lab coordinated by Professor Hermi F. Brito (IQ/USP) is acknowledged for some PL measurements.

Appendix A. Supporting information

Supplementary data associated with this article can be found in the online version at doi:10.1016/j.materresbull.2026.114282.

Data availability

Data will be made available on request.

References

[1] E.J. Green, W.E. Weber, Will the new $100 bill decrease counterfeiting? Fed. Reserve Bank. Minneap. Q. Rev. 20 (1996) 3–10, https://doi.org/10.21034/wp.571.
[2] E. Quercioli, L. Smith, The economics of counterfeiting, Econometrica 83 (2015) 1211–1236, https://doi.org/10.3982/ECTA10975.
[3] S. Huang, A. Mukundan, Y. Tsao, Y. Kim, F. Lin, H. Wang, Recent advances in counterfeit art, document, photo, hologram, and currency detection using hyperspectral imaging, Sensors 22 (2022) 7308, https://doi.org/10.3390/s22197308.
[4] A. Polak, T. Kelman, P. Murray, S. Marshall, D.J.M. Stothard, N. Eastaugh, F. Eastaugh, Hyperspectral imaging combined with data classification techniques as an aid for artwork authentication, J. Cult. Herit. 26 (2017) 1–11, https://doi.org/10.1016/j.culher.2017.01.013.
[5] C.S. Silva, M.F. Pimentel, R.S. Honorato, C. Pasquini, J.M. Prats-Montalbán, A. Ferrer, Near infrared hyperspectral imaging for forensic analysis of document forgery, Analyst 139 (2014) 5176–5184, https://doi.org/10.1039/C4AN00961D.
[6] T.P. Nguyen, H.P. Dang, L.G. Nguyen, C.D. Le, Synthesis of ZnO nanoparticles-based fluorescent ink for information encryption and security applications, Opt. Mater. 157 (2024) 116296, https://doi.org/10.1016/j.optmat.2024.116296.
[7] S.C. Kim, J.H. Park, S.O. Chin, J. Kim, D. Kim, Recent advances in anti-counterfeiting technology using fluorescent hybrid materials, Adv. Compos. Hybrid. Mater. (2025), https://doi.org/10.1007/s42114-025-01534-4.
[8] X. Liang, F. Zhang, H. Gong, R. Wei, H. Guo, F. Hu, Dual-mode optical thermometry and multilevel anti-counterfeiting based on Er^{3+}/Eu^{3+} doped $Ba_5Gd_8Zn_4O_{21}$ phosphors, J. Lumin. 269 (2024) 120483, https://doi.org/10.1016/j.jlumin.2024.120483.
[9] X. Zhou, L. Ning, J. Qiao, Y. Zhao, P. Xiong, Z. Xia, Interplay of defect levels and rare earth emission centers in multimode luminescent phosphors, Nat. Commun. 13 (2022) 7589, https://doi.org/10.1038/s41467-022-35366-3.
[10] C.W. Thiel, T. Bottger, R.L. Cone, Rare-earth-doped materials for applications in quantum information storage and signal processing, J. Lumin. 131 (2011) 353–361, https://doi.org/10.1016/j.jlumin.2010.12.015.
[11] P.C. Sousa Filho, J.F. Lima, O.A. Serra, From lighting to photoprotection: fundamentals and applications of rare earth materials, J. Braz. Chem. Soc. 26 (2015) 2471–2495, https://doi.org/10.5935/0103-5053.20150328.
[12] T.P. Pereira, F.S.M. Canisares, J.H. Araujo-Neto, J. Ellena, L.C.V. Rodrigues, H. F. Brito, A.G. Bispo-Jr, Dual spectral and temporal encoding in luminescent polymeric films using a Eu^{III} complex and a persistent phosphor for anticounterfeiting applications, J. Mater. Chem. C. 13 (2025) 19788–19796, https://doi.org/10.1039/D5TC02512E.
[13] D. Guo, H. Suo, J. Zhao, K. Li, Y. Zhang, R. Lu, Z. Fu, Brightening full-spectrum lanthanide mechanoluminescence in a wurtzite semiconductor via structural reconstruction, 202502712, Laser Photonics Rev. (2025), https://doi.org/10.1002/lpor.202502712.
[14] Y. Wang, P. Dang, Z. Zeng, D. Liu, G. Zhang, L. Tian, K. Li, P. Ma, Y. Wei, H. Lian, Z. Hou, G. Li, J. Lin, Sensitizing effect of lanthanide luminescence by Mo^{4+}/Ag^{+} in double perovskites: great enhancement of near-infrared emission via wide range of excitation (250–850 nm), Light. Sci. Appl. 14 (2025), https://doi.org/10.1038/s41377-025-02159-4.
[15] H.Q. Wang, M. Batentschuk, A. Osvet, L. Pinna, C.J. Brabec, Rare-earth ion doped up-conversion materials for photovoltaic applications, Adv. Mater. 23 (2011) 2675–2680, https://doi.org/10.1002/adma.201100511.
[16] J. Zhang, Z. Wang, X. Huo, X. Meng, Y. Wang, H. Suo, P. Li, Anti-counterfeiting application of persistent luminescence materials and its research progress, Laser Photonics Rev. 18 (2024) 2300751, https://doi.org/10.1002/lpor.202300751.
[17] C. Zhang, Q. Yin, S. Ge, J. Qi, Q. Han, W. Gao, Y. Wang, M. Zhang, J. Dong, Optical anti-counterfeiting and information storage based on rare-earth-doped luminescent materials, Mater. Res. Bull. 176 (2024) 112801, https://doi.org/10.1016/j.materresbull.2024.112801.
[18] Y. Wang, J. Chang, C. Chen, Y. Wu, R. Gao, J. Li, C. Guo, Dynamic tunable multifunctional platform $BiOCl:Yb^{3+}/Ho^{3+}$ with multimodal photo-response for intelligent anti-counterfeiting, Adv. Funct. Mater. 202528912 (2026), https://doi.org/10.1002/adfm.202528912.
[19] Y. Li, H. Du, Y. Ma, M. Liu, J. Zou, S. Wang, J. Yang, S. Hu, Lin, J., Correction: Construction of energy transfer channels from $[SbCl_6]^{3-}$ to Ln^{3+} (Ln^{3+} = Ho^{3+}, Er^{3+}) in $Cs_2NaGdCl_6$ for advanced anti-counterfeiting materials, J. Mater. Chem. C. (2024), https://doi.org/10.1039/D4TC90143F.
[20] M. Xu, W. Ge, J. Shi, Y. Wu, Y. Li, Stretchable and flexible $Bi_2Ti_4O_{11}:Yb^{3+},Er^{3+}$@TPU film stimulated by near infrared for dynamic and multimodal anti-counterfeiting, J. Alloy. Compd. 885 (2021) 161164, https://doi.org/10.1016/j.jallcom.2021.161164.
[21] P.P. Pradhan, D. Haranath, A luminescent pathway for anti-counterfeiting of currency and forensic applications, J. Rare Earths 164 (2024) 67–142, https://doi.org/10.21741/9781644903056-2.
[22] P. Kumar, J. Dwivedi, B.K. Gupta, Highly luminescent dual mode rare-earth nanorod assisted multi-stage excitable security ink for anti-counterfeiting applications, J. Mater. Chem. C. 2 (2014) 10468–10475, https://doi.org/10.1039/C4TC02065K.
[23] J. Liu, B. Chen, Q. Zhu, Coating red phosphor on green luminescent material for multi-mode luminescence and advanced anti-counterfeit applications, Coatings 14 (2024) 509, https://doi.org/10.3390/coatings14040509.
[24] A.I. Kostyukov, N.Y. Kostyukova, A.A. Nashivochnikov, M.I. Rakhmanova, E. A. Suprun, Photoluminescent $Y_2O_3:Eu^{3+}$@PVA composite dispersions and films for anti-counterfeiting ink applications, Opt. Mater. 157 (2024) 116194, https://doi.org/10.1016/j.optmat.2024.116194.
[25] B. Song, M. Wang, Y. Zhong, B. Chu, Y. Su, Y. He, Fluorescent and magnetic anti-counterfeiting realized by biocompatible multifunctional silicon nanoshuttle-based security ink, Nanoscale 10 (2018) 1617–1621, https://doi.org/10.1039/C7NR06337G.
[26] P. Jain, D. Gupta, H. Kaur, S. Singh, K.K. Gaikwad, Advanced anti-counterfeit inks in food packaging: A comprehensive review focusing on functional materials to digital integration, Trends Food Sci. Technol. 164 (2025) 105229, https://doi.org/10.1016/j.tifs.2025.105229.
[27] Kanika, G. Kedawat, S. Singh, B.K. Gupta, A novel approach to design luminomagnetic pigment formulated security ink for manifold protection to bank cheques against counterfeiting, Adv. Mater. Technol. 6 (2021) 2000973, https://doi.org/10.1002/admt.202000973.
[28] P. Woźny, K. Soler-Carracedo, M. Perzanowski, J. Moszczyński, S. Lis, M. Runowski, Bifunctional upconverting luminescent-magnetic FeS_2@$NaYF_4:Yb^{3+}$, Er^{3+} core@shell nanocomposites with tunable luminescence for temperature sensing, J. Mater. Chem. C. 12 (2024) 11824–11835, https://doi.org/10.1039/D4TC01117A.
[29] A.L. Costa, C.J. Pacheco, J.C. Patiño, A.M.S. Gomes, F. Artizzu, S.A.M. Lima, A. G. Bispo-Jr, A.M. Pires, A dual-mode magnetic–luminescent hybrid: $Fe_3O_4 + Y_2O_3:Yb^{3+},Tm^{3+}$ decorated with a Eu^{3+} β-diketonate complex, Mater. Res. Bull. (2025) 113943, https://doi.org/10.1016/j.materresbull.2025.113943.
[30] D. Llamosa Pérez, I. Puentes, G.A. Murillo Romero, I.M. Saavedra Gaona, C. A. Parra Vargas, R.J. Rincón, Synthesis of superparamagnetic iron oxide nanoparticles coated with polyethylene glycol as potential drug carriers for cancer treatment, J. Nanopart. Res. 26 (2024) 2, https://doi.org/10.1007/s11051-023-05900-5.
[31] S. Kumar, H. Tripathi, S. Bhardwaj, D. Garbiec, A. Gupta, U. Batra, J.D. Sharma, Structural and opto-electrical properties of Y_2O_3 nanopowders synthesized by co-precipitation method, J. Mol. Struct. 1302 (2024) 137463, https://doi.org/10.1016/j.molstruc.2023.137463.
[32] T.K. Anh, P. Benalloul, C. Barthou, L.T. Giang, N. Vu, L. Minh, Luminescence, energy transfer, and upconversion mechanisms of Y_2O_3 nanomaterials doped with Eu^{3+}, Tb^{3+}, Tm^{3+}, Er^{3+}, and Yb^{3+} ions, J. Nanomater. 2007 (2007) 48247, https://doi.org/10.1155/2007/48247.
[33] S.O. Lira, C. Burda, A. Franco Jr., Effects of rare earth doping on the structural and dielectric properties of sodium bismuth titanate perovskites, SSRN Electron. J. (2024), https://doi.org/10.1016/j.jpcs.2024.112133.
[34] M. Yang, Y. Sui, S. Wang, X. Wang, Y. Wang, S. Lü, T. Lü, W. Liu, Correlation between the surface state and optical properties of S_6 site and C_2 site in nanocrystalline $Eu^{3+}:Y_2O_3$, J. Alloy. Compd. 509 (2011) 266–270, https://doi.org/10.1016/j.jallcom.2010.07.088.
[35] S. Laurent, D. Forge, M. Port, A. Roch, C. Robic, L. Vander Elst, R.N. Muller, Magnetic iron oxide nanoparticles: synthesis, stabilization, vectorization, physicochemical characterizations, and biological applications, Chem. Rev. 108 (2008) 2064–2110, https://doi.org/10.1021/cr900197g.
[36] B.D. Cullity, S.R. Stock, *Elements of X-Ray Diffraction*, 3rd ed, Prentice Hall,, Upper Saddle River, 2014.
[37] S. Ilyas, Heryanto, B. Abdullah, D. Tahir, X-ray diffraction analysis of nanocomposite Fe_3O_4/activated carbon by Williamson–Hall and size-strain plot methods, Nano-Struct. Nano-Objects 20 (2019) 100396, https://doi.org/10.1016/j.nanoso.2019.100396.
[38] P. Soltanpour, R. Naderali, Mabhouti, Kh., Comparative study on structural, morphological, and optical properties of MS/Fe_3O_4 nanocomposites and M-doped

Fe_3O_4 nanopowders (M = Mn, Zn), Sci. Rep. 14 (2024) 21287, https://doi.org/10.1038/s41598-024-72026-6.
[39] S. Husain, M. Irfansyah, N.H. Haryanti, S. Suryajaya, S. Arjo, A. Maddu, Synthesis and characterization of Fe_3O_4 magnetic nanoparticles from iron ore, J. Phys. Conf. Ser. 1153 (2019) 012021, https://doi.org/10.1088/1742-6596/1242/1/012021.
[40] H. Lee, S. Hwang, S. Lee, K.H. Hong, H.M. Oh, Y.J. Park, H.N. Kim, T.J. Yu, Measurement of Nd:Y_2O_3 broad band near infra-red transmittance using FTIR system, Opt. Mater. 143 (2023) 114227, https://doi.org/10.1016/j.optmat.2023.114227.
[41] S. Koçak Soylu, O.S. Özdemir, M. Asiltürk, I. Atmaca, Thermal and optical characteristics of TiO_2@SiO_2, Fe_3O_4@SiO_2, and ZnO@SiO_2 core–shell nanoparticles and their water-based nanofluids, Int. J. Thermophys. 46 (2025) 1–31, https://doi.org/10.1007/s10765-025-03558-w.
[42] K.I. Hadjiivanov, D.A. Panayotov, M.Y. Mihaylov, E.Z. Ivanova, K.K. Chakarova, S. M. Andonova, N.L. Drenchev, Power of infrared and Raman spectroscopies to characterize metal-organic frameworks and investigate their interaction with guest molecules, Chem. Rev. 121 (2021) 1286–1424, https://doi.org/10.1021/acs.chemrev.0c00487.
[43] K. Saito, T. Xu, H. Ishikita, Correlation between C=O stretching vibrational frequency and pKa shift of carboxylic acids, J. Phys. Chem. B 126 (2022) 4999–5006, https://doi.org/10.1021/acs.jpcb.2c02193.
[44] T.A. Kovacs, M.C.F.C. Felinto, T.B. Paolini, B. Ali, L.K.O. Nakamura, E.E. S. Teotonio, H.F. Brito, O.L. Malta, Synthesis and photoluminescence properties of [Eu(dbm)$_3$PX] and [Eu(acac)$_3$·PX] complexes, J. Lumin. 193 (2018) 98–105, https://doi.org/10.1016/j.jlumin.2017.09.029.
[45] J.A.O. Santos, A.M.G. Mutti, A.G. Bispo-Jr, A.M. Pires, S.A.M. Lima, Red-emitting hybrid based on Eu^{3+}-dbm complex anchored on silica nanoparticles surface by carboxylic acid for biomarker application, Materials 13 (2020) 5494, https://doi.org/10.3390/ma13235494.
[46] W. Wu, C.Z. Jiang, V.A.L. Roy, Designed synthesis and surface engineering strategies of magnetic iron oxide nanoparticles for biomedical applications, Nanoscale 8 (2016) 19421–19474, https://doi.org/10.1039/C6NR07542H.
[47] I. Sharifi, H. Shokrollahi, S. Amiri, Ferrite-based magnetic nanofluids used in hyperthermia applications, J. Magn. Magn. Mater. 324 (2012) 903–915, https://doi.org/10.1016/j.jmmm.2011.10.017.
[48] N.V.S. Vallabani, S. Singh, A.S. Karakoti, Magnetic nanoparticles: current trends and future aspects in diagnostics and nanomedicine, Curr. Drug. Metab. 20 (2019) 457–472, https://doi.org/10.2174/1389200220666181122124458.
[49] I.E. Kolesnikov, M.A. Kurochkin, E.I. Shuvarakova, A.A. Nashivochnikov, A. I. Kostyukov, Boltzmann thermometry: Eu^{3+}-doped monoclinic Y_2O_3 and Y_2O_3@SiO_2 nanoparticles, Ceram. Int. 51 (2025) 16904–16911, https://doi.org/10.1016/j.ceramint.2024.08.227.
[50] Q. Han, T. Yan, Y. Song, Y. Wang, X. Zhang, Up-conversion luminescence enhancement and tunable emission color of Y_2O_3:Tm/Yb@Y_2O_3:Yb@Y_2O_3:Er/Yb multilayer thin films, J. Alloy. Compd. 877 (2021) 160151, https://doi.org/10.1016/j.jallcom.2021.160151.
[51] X.H. Liu, W. Liu, Z.D. Zhang, Extremely low coercivity in Fe_3O_4 thin film grown on Mg_2TiO_4 (001), RSC Adv. 7 (2017) 43648–43654, https://doi.org/10.1039/C7RA08916C.
[52] Q. Li, C.W. Kartikowati, S. Horie, T. Ogi, T. Iwaki, K. Okuyama, Correlation between particle size/domain structure and magnetic properties of highly crystalline Fe_3O_4 nanoparticles, Sci. Rep. 7 (2017) 9894, https://doi.org/10.1038/s41598-017-09897-5.
[53] H. Peng, B. Cui, Y. Wang, Bifunctional Fe_3O_4@Gd_2O_3:Eu^{3+} nanocomposites obtained by the homogeneous precipitation method, Mater. Res. Bull. 48 (2013) 1767–1771, https://doi.org/10.1016/j.materresbull.2013.01.001.
[54] B. Li, H. Fan, Q. Zhao, C. Wang, Synthesis, characterization and cytotoxicity of novel multifunctional Fe_3O_4@SiO_2@$GdVO_4$:Dy^{3+} core-shell nanocomposite as a drug carrier, Materials 9 (2016) 149, https://doi.org/10.3390/ma9030149.
[55] R. Dawn, M. Zzaman, F. Faizal, C. Kiran, A. Kumari, R. Shahid, C. Panatarani, I. M. Joni, V.K. Verma, S.K. Sahoo, K. Amemiya, V.R. Singh, Origin of magnetization in silica-coated Fe_3O_4 nanoparticles revealed by soft X-ray magnetic circular dichroism, Braz. J. Phys. 52 (2022) 99, https://doi.org/10.1007/s13538-022-01102-x.
[56] C. Mayrinck, R.L. Siqueira, J. Esbenshade, M.A. Schiavon, R.C. de Lima, H. P. Barbosa, S.J.L. Ribeiro, J.L. Ferrari, Downconversion and upconversion observed from Er^{3+}/Yb^{3+}/Eu^{3+} tri-doped Y_2O_3 for application in energy conversion, J. Alloy. Compd. 816 (2020) 152591, https://doi.org/10.1016/j.jallcom.2019.152591.
[57] X. Yang, Z. Wu, Z. Yang, X. Zhao, C. Song, M. Yuan, K. Han, H. Wang, S. Li, X. Xu, Flame-made Y_2O_3:Yb^{3+}/Er^{3+} upconversion nanoparticles: mass production synthesis, multicolor tuning and thermal sensing studies, J. Alloy. Compd. 854 (2021) 157078, https://doi.org/10.1016/j.jallcom.2020.157078.
[58] G. Bilir, O. Erguzel, Up-conversion emission properties and unexpected white light emission from Er^{3+}/Yb^{3+} doped Gd_2O_3 nanophosphors, Mater. Res. Express 3 (2016) 106201, https://doi.org/10.1088/2053-1591/3/10/106201.
[59] A.C. Brandão-Silva, M.A. Gomes, S.M.V. Novais, Z.S. Macedo, J.F.M. Avila, J. J. Rodrigues Jr., M.A.R.C. Alencar, Size influence on temperature sensing of erbium-doped yttrium oxide nanocrystals exploiting thermally coupled and uncoupled levels' pairs, J. Alloy. Compd. 731 (2018) 478–488, https://doi.org/10.1016/j.jallcom.2017.09.156.
[60] P. Thokwane, P. Mbule, Analysis of the $NaYF_4$:Yb^{3+},Er^{3+} nanocrystals: up-conversion luminescence, crystal structure and morphology influenced by the dopant concentration and annealing temperature, Bull. Mater. Sci. 46 (2023) 140, https://doi.org/10.1007/s12034-023-02978-4.
[61] G.B. Nair, S. Tamboli, S.J. Dhoble, H.C. Swart, LaOF:Yb^{3+},Er^{3+} upconversion nanophosphors operating at low laser powers for nanothermometry applications, ACS Appl. Nano Mater. 6 (2023) 15255–15265, https://doi.org/10.1021/acsanm.3c03208.
[62] C.M.B. Leite Silva, A.G. Bispo-Jr, F.S.M. Canisares, S.A. Castilho, S.A.M. Lima, A. M. Pires, Eu^{3+}-tetrakis β-diketonate complexes for solid-state lighting application, Luminescence 34 (2019) 877–886, https://doi.org/10.1002/bio.3686.
[63] L. Ruan, X. Gao, J. Zhao, C. Xu, D. Liang, Preparation and characteristics of Eu(DBM)$_3$phen: synthesis, single-crystal structure and spectroscopic analysis, J. Mol. Struct. 1149 (2017) 265–272, https://doi.org/10.1016/j.molstruc.2017.08.003.
[64] N. Hasan, K. Iftikhar, Synthesis, crystal structure and photoluminescence studies of [Eu(dbm)$_3$(impy)] and its polymer-based hybrid film, New. J. Chem. 43 (2019) 2479–2489, https://doi.org/10.1039/C8NJ04560G.
[65] J.L. Cervantes, L.A. Diaz-Torres, J. Elias, M.A. Vallejo, J. Hernández-Paredes, Structural, morphological and photoluminescent study of SiO_2–Y_2O_3 doped with Er^{3+} and Yb^{3+} with enhanced up-conversion emission, Appl. Phys. A 131 (2025) 599, https://doi.org/10.1007/s00339-025-08718-1.
[66] T. López-Luke, E. De la Rosa, I. Campos Villalobos, R.A. Rodriguez, C. Ángles-Chávez, P. Salas, D.A. Wheeler, J.Z. Zhang, Improving pure red upconversion emission of Co-doped Y_2O_3:Yb^{3+}–Er^{3+} nanocrystals with a combination of sodium sulfide and surfactant Pluronic-F127, J. Lumin. 145 (2014) 292–298, https://doi.org/10.1016/j.jlumin.2013.07.012.
[67] B. Xu, C. Song, R. Huang, J. Song, Z. Lin, J. Song, J. Liu, Luminescence properties related to energy transfer process and cross relaxation process of Y_2O_3:Yb^{3+}/Er^{3+} thin films doped with K^+ ion, Opt. Mater. 118 (2021) 111290, https://doi.org/10.1016/j.optmat.2021.111290.
[68] L.F. Saraiva, A.N. Carneiro Neto, A.G. Bispo-Jr, M.M. Quintano, E. Kraka, L. D. Carlos, S.A.M. Lima, A.M. Pires, R.T. Moura Jr., Role of vibronic coupling for the dynamics of intersystem crossing in Eu^{3+} complexes: an avenue for brighter compounds, J. Chem. Theory Comput. 21 (2025) 3066–3076, https://doi.org/10.1021/acs.jctc.4c01461.
[69] Z. Ahmed, R.S. Carvalho, A.M. dos Santos, F. Gambassi, E. Bandini, L. Marvelli, L. Maini, A. Barbieri, M. Cremona, Highly luminescent europium(III) complexes in solution and PMMA-doped films for bright red electroluminescent devices, Molecules 28 (2023) 4371, https://doi.org/10.3390/molecules28114371.
[70] R. Shi, A.-V. Mudring, Phonon-mediated nonradiative relaxation in Ln^{3+}-doped luminescent nanocrystals, ACS Mater. Lett. 4 (2022) 1882–1903, https://doi.org/10.1021/acsmaterialslett.2c00595.
[71] I.L.V. Rosa, P.C. de Sousa Filho, C.R. Neri, O.A. Serra, A.T. de Figueiredo, J. A. Varela, E. Longo, Synthesis and study of the photophysical properties of a new Eu^{3+} complex with 3-hydroxypicolinamide, J. Fluoresc. 21 (2011) 1575–1583, https://doi.org/10.1007/s10895-011-0846-y.
[72] K.-L. Wong, J.-C.G. Bünzli, P.A. Tanner, Quantum yield and brightness, J. Lumin. 224 (2020) 117256, https://doi.org/10.1016/j.jlumin.2020.117256.
[73] C.M.B. Leite Silva, A.G. Bispo-Jr, S.A.M. Lima, A.M. Pires, Eu^{3+} complex/polymer films for light-emitting diode applications, Opt. Mater. 96 (2019) 109323, https://doi.org/10.1016/j.optmat.2019.109323.
[74] H. Li, Y. Chen, T. Wang, L. Liu, B. Zhang, Y. Wang, D. Yang, Ternary Eu^{3+} crystalline complexes with photoluminescence and triboluminescence for dynamic stress visualization, J. Colloid Interface Sci. 670 (2024) 530–539, https://doi.org/10.1016/j.jcis.2024.05.110.
[75] A.M.G. Mutti, F.S.M. Canisares, J.A.O. Santos, B.C. Santos, D.G.S.M. Cavalcante, A. E. Job, A.M. Pires, S.A.M. Lima, Silica-based nanohybrids containing europium complexes covalently grafted: structural, luminescent, and cell labeling investigation, J. Sol. -Gel Sci. Technol. 107 (2023) 754–770, https://doi.org/10.1007/s10971-023-06138-2.